

Atomically isolated copper on titanium dioxide for ammonia photosynthesis via nitrate reduction with unprecedently high apparent quantum yield

Hyun Sik Moon^{a,h}, Byeongju Song^{b,h}, Jiwon Jeon^{c,h}, Ting-Hsuan Lai^{d,e}, Yu-Peng Chang^{d,e}, Yi-Dong Lin^{e,f}, Jun Kue Park^g, Yan-Gu Lin^{e,f}, Yung-Jung Hsu^{d,e}, Hyeyoung Shin^{c,h}, Yongju Yun^{b,h}, Kijung Yong^{a,h,*}

^a Surface Chemistry Laboratory of Electronic Materials, Department of Chemical Engineering, Pohang University of Science and Technology (POSTECH), Pohang 37673, the Republic of Korea

^b Nanocatalysis and Surface Science Laboratory, Department of Chemical Engineering, Pohang University of Science and Technology (POSTECH), Pohang 37673, the Republic of Korea

^c Graduate School of Energy Science and Technology (GEST), Chungnam National University, Daejeon 34134, the Republic of Korea

^d Department of Materials Science and Engineering, National Yang Ming Chiao Tung University, Hsinchu 300093, Taiwan

^e Center for Emergent Functional Matter Science, National Yang Ming Chiao Tung University, Hsinchu 300093, Taiwan

^f Scientific Research Division, National Synchrotron Radiation Research Center, Hsinchu 30076, Taiwan

^g Korea Multi-purpose Accelerator Complex, Korea Atomic Energy Research Institute, Gyeongju 38180, the Republic of Korea

^h Research Center for Carbon-zero Green Ammonia Cycling, Pohang University of Science and Technology (POSTECH), Pohang 37673, the Republic of Korea

ARTICLE INFO

Keywords:

Solar fuel production
Single-atom catalyst
2D nanosheet structure
Hydrogen carrier
Photocatalysis

ABSTRACT

Photocatalytic nitrate (NO_3^-) reduction to NH_3 (PcNRA) is a sustainable alternative that is considered advantageous over N_2 fixation, which suffers from the high dissociation energy and sluggish activation of inactive N_2 . Although PcNRA has recently been shown to achieve excellent selectivity, its sluggish kinetics restrict the NH_3 production efficiency. Herein, we present a single-atom Cu-incorporated TiO_2 nanosheet (Cu-TNS) photocatalyst for efficient and selective PcNRA. Single Cu atoms displacing Ti sites accumulate photogenerated electrons, ensuring efficient charge separation and surface NO_3^- reduction. Moreover, introducing Cu atoms into the TiO_2 matrix induces spontaneous defect formation, resulting in oxygen vacancies and lattice strain that promote NO_3^- adsorption and activation. The simultaneous presence of single Cu atoms and structural defects in Cu-TNS synergistically stimulates PcNRA, leading to a 62-fold enhancement over pristine TiO_2 in NH_3 production with 97.6% selectivity and an unprecedently high apparent quantum yield of 11.7% at 330 nm under optimized conditions.

1. Introduction

Ammonia (NH_3 or NH_4^+), one of the most produced and utilized chemicals, is an indispensable feedstock for nitrogen-based fertilizers and is recently considered an ideal carbon-neutral fuel or hydrogen carrier with an intensely high hydrogen density [1–3]. Unfortunately, current NH_3 manufacturing primarily relies on the energy-consuming (1.0–2.0% of the world's energy output) and waste-intensive (1.5% of the world's carbon emission) Haber-Bosch process [4,5]. Among the environmentally-friendly and thus sustainable alternatives,

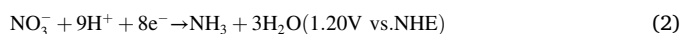
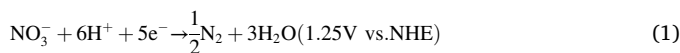
photocatalytic nitrate (NO_3^-) reduction to ammonia (PcNRA) is a favorable opportunity for green NH_3 production. The relatively low dissociation energy of the N = O bond (204 kJ mol⁻¹) and the high aqueous solubility of NO_3^- could readily exempt the fatal bottleneck of N_2 fixation [6–8] and sufficient NH_3 yields eliminate the possibility of false positives [9,10]. As another virtue, NO_3^- as well as general organic matters acting as hole scavengers are abundantly prevalent as major pollutants in wastewater [11,12]. Therefore, PcNRA, which degrades contaminants via sunlight to produce value-added chemicals and accelerates reaction kinetics, offers a promising avenue to simultaneously

* Corresponding author at: Surface Chemistry Laboratory of Electronic Materials, Department of Chemical Engineering, Pohang University of Science and Technology (POSTECH), Pohang 37673, the Republic of Korea.

E-mail address: kyong@postech.ac.kr (K. Yong).

address energy and environmental concerns [13].

PcNRA has two possible pathways: N₂ formation via 5e⁻ reduction (Eq. (1)) and NH₃ formation via 8e⁻ reduction (Eq. (2)) [14]. The hydrogen evolution reaction (Eq. (3)), a fierce side-reaction that consumes photoexcited electrons, is another consideration [15,16]. Accordingly, PcNRA is thermodynamically and kinetically unfavorable, and thus the majority of previous NO₃⁻ reduction studies have been focused on N₂ formation as a water treatment [17–19]. To the best of our knowledge, only a few photocatalysts for selective PcNRA, such as titanium dioxide (TiO₂) with surface oxygen vacancies (OVs) [14] or decorated with metallic [20], bimetallic [21] or metal oxide [22,23] clusters, have been reported. Although 96–98% selectivity toward NH₃ synthesis has been reported, the actual catalytic activities have still been far below the practical standard due to the sluggish reaction kinetics (the highest apparent quantum yield (AQY) of 3.5% (at $\lambda = 525$ nm)) [22]. Therefore, the design of an efficient photocatalyst for selective NH₃ production is highly desirable.



Recently, single-atom catalysts (SACs) have been intensely investigated as a breakthrough in the inefficiency of photocatalysis because the isolated metal atoms provide more active sites and reactant-molecule adsorption [24,25]. So far, although SACs have been studied for various photocatalysis such as H₂ evolution [26–28], CO₂ conversion [29] and organic pollutant degradation [30,31], the impact of SACs on PcNRA has not yet been fully exploited. Among the SAC candidates, Cu, one of the earth-abundant transition metals, has shown impressive selectivity and activity for photo-/electrochemical NH₃ synthesis due to its unique properties [20,21,32,33]. Its volatile valence state ensures efficient charge separation, leading to higher catalytic activity compared to even noble metal-loaded photocatalysts [34]. Therefore, incorporating Cu atoms into a light-responsive metal oxide lattice could be a guaranteed strategy to maximize the catalytic activity and selectivity of SACs for PcNRA. Moreover, this strategy may induce the formation of OVs and lattice strain due to the different valence states of the metal and support, which further stimulates adsorption and activation of the reactant-molecules [35,36].

Following the above hypothesis, we designed and synthesized single-atom Cu-introduced TiO₂ nanosheets (Cu-TNS) for efficient and selective PcNRA under ambient conditions. Through a bottom-up approach, single Cu atoms were uniformly distributed in the TiO₂ matrix by displacing Ti sites. The site-specific-incorporated single Cu atoms exhibited a high oxidation state resulting from a high unoccupied state level, which induced the localization of photogenerated electrons at the single Cu sites, effectively boosting charge separation. In particular, structural defects such as OV and lattice strain spontaneously occurred in the vicinity of stabilized Cu atoms, which delivered favorable NO₃⁻ adsorption sites and thereby eliminated the activation barrier. Thanks to the concurrent existence of single Cu atoms and defects in the TiO₂ matrix, Cu-TNS exhibited a 62-fold enhanced NH₄⁺ production rate with 97.6% selectivity compared to pristine TiO₂ nanosheets (TNS). Moreover, Cu-TNS exhibited an AQY of 11.7% at 330 nm under optimized reaction conditions, far surpassing that of the current state-of-the-art photocatalyst for PcNRA [22].

2. Experimental section

2.1. Materials

Tetrabutyl titanate (TBOT, ≥99.0%), copper nitrate trihydrate (Cu(NO₃)₂·3 H₂O, 99.9%), hydrofluoric acid (HF, 37 wt%), iodine (I₂,

99.5%), acetone (CH₃COCH₃, 96%), methanol (CH₃OH, ≥99.0%), ethylene glycol (anhydrous, 99.8%) formic acid (HCOOH, ≥95.0%), potassium nitrate (KNO₃, ≥99.0%), potassium nitrate-¹⁵N (K¹⁵NO₃, 98 atom%), potassium sulfate (K₂SO₄, ≥99.0%), maleic acid (C₄H₄O₄, ≥99.0%), ammonium chloride (NH₄Cl, ≥99.5%), and ammonium-¹⁵N chloride (¹⁵NH₄Cl, ≥98 atom%) were purchased from Sigma Aldrich. Absolute ethanol was purchased from Fisher Scientific Korea Ltd. (Seoul, Korea). All chemicals were obtained from commercial suppliers and used without further purification.

2.2. Photocatalysts synthesis

The Cu-TNS, oxygen-deficient TiO₂ nanosheets (OV-TNS), and pristine TiO₂ nanosheets (TNS) photocatalysts were synthesized by using the solvothermal method [37] with modifications. In a typical synthetic process, 5 mL of TBOT were mixed with 0.6 mL of HF, 20 mL of absolute ethanol, and a calculated amount of Cu(NO₃)₂·3 H₂O (a specific at% of Cu relative to Ti), followed by stirring for 30 min. The solution was then transferred into a Teflon-lined stainless steel autoclave and heated in an oven at 180 °C for 4 h. The final product was centrifuged, washed repeatedly with DI water, and dried at 60 °C overnight. OV-TNS was synthesized following the above procedure without Cu(NO₃)₂·3 H₂O, where oxygen vacancies are present due to the nature of the 2D nanosheet structure [35]. TNS was synthesized by calcination of OV-TNS at 300 °C for 2 h to remove oxygen vacancies and obtain higher crystallinity. A CuNP/TNS photocatalyst was prepared via photo-reduction method. 50 mg of TNS was dispersed in 25 mL of 20 vol% aqueous methanol solution, containing 4.7 mg (3 at%) of Cu(NO₃)₂·3 H₂O. The mixture was stirred for 1 h under dark condition to achieve adsorption/desorption equilibrium. The suspension was then irradiated with 300-W Xe lamp (Newport) for 6 h under vigorous stirring. The final product was centrifuged, washed with DI water and finally dried at 60 °C overnight.

2.3. Characterization, calculation, and photocatalytic reaction

The characterization, calculation, and photocatalytic reaction details for the prepared catalysts are described in the [Supporting Information](#).

3. Results and discussion

3.1. Characterization of Cu-TNS

Cu-TNS and counterpart photocatalysts, pristine TNS OV-TNS, were prepared using a facile solvothermal method to substantiate the contributions of each feature. The morphology of Cu-TNS was investigated via transmission electron microscopy (TEM) and scanning electron microscopy, revealing ultra-thin nanosheet structures with a lateral length of ~10 nm and a thickness of ~2.3 nm (Fig. 1a, b and Fig. S1). Lattice spacing measurements in the high-resolution (HR)TEM images reveal that the top and bottom facets are the (001) planes and the side facets are the (200) and (020) planes of anatase TiO₂, indicating that reactive (001) facets [37] are predominantly exposed in Cu-TNS (Fig. S2). Electron energy loss spectroscopy and scanning TEM energy dispersive X-ray spectroscopy (STEM-EDS) analyses show an even distribution of Cu species on the TNS without aggregation (Fig. 1c and Fig. S3). TNS and OV-TNS without Cu species have similar nanosheet structures, of which TNS is slightly larger with distinct grain contours due to high crystallinity without defects (Figs. S4–6), which is consistently evidenced by the slightly reduced surface area of TNS (Fig. S7).

High-angle annular dark-field (HAADF)-STEM analysis was performed to gain in-depth insight into the localized atomic structure of Cu-TNS. The bright contrast spots evident at the Ti atomic sites imply that the Cu atoms in the Ti vacancies are particularly stable and other configurations such as clusters or new phases did not occur (Fig. 1d–g). The corresponding line scan profile of the marked area further affirms

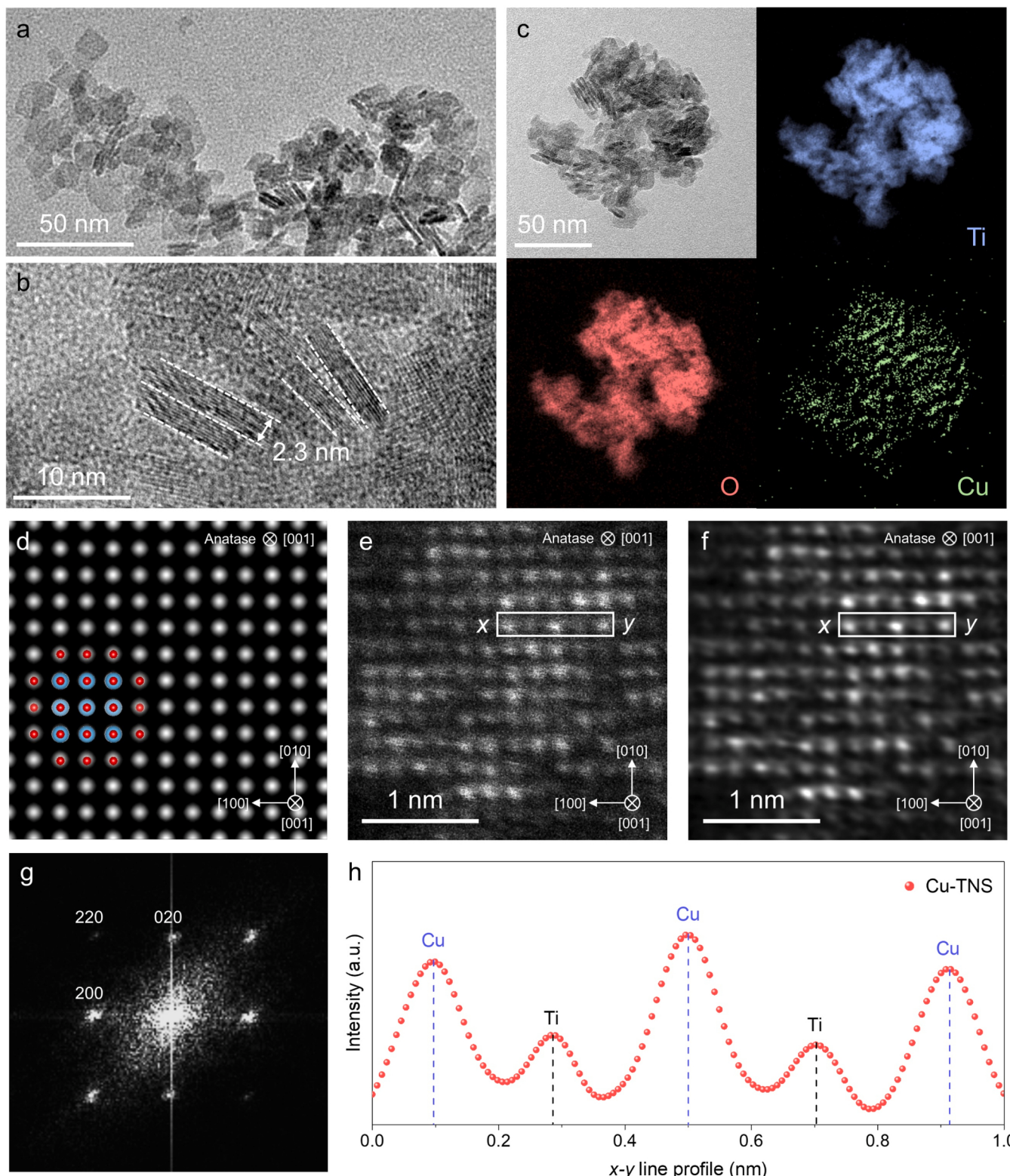


Fig. 1. Representative (a), (b) TEM images and (c) an EELS elemental mapping (Ti, O and Cu) image of Cu-TNS. HAADF-STEM images of Cu-TNS in the [001] direction: (d) a simulated image of anatase TiO_2 showing the corresponding anatase TiO_2 unit cell structure in which the blue and red spheres represent Ti and O, respectively; (e) a Cs-corrected raw image; (f) a filtered image and (g) the corresponding fast Fourier transform pattern. (h) The x–y line scan profile of the marked areas in (e) and (f).

distinct intensity differences that suggest stabilization of the Cu atoms in the TiO_2 matrix by forming Cu–O–Ti bonds (Fig. 1h). Subsequently, X-ray absorption spectroscopy (XAS) was performed to statistically analyze the comprehensive atomic structure of Cu-TNS. The Cu K-edge

X-ray absorption near-edge structure (XANES) spectrum in Fig. 2a exhibits the typical characteristic absorption edges of the Cu^{2+} valence state [26] at 8988.2 and 8997.5 eV. Moreover, the Cu^0 and Cu^{1+} valence states in Cu-TNS were not present, unlike in the reference XANES spectra

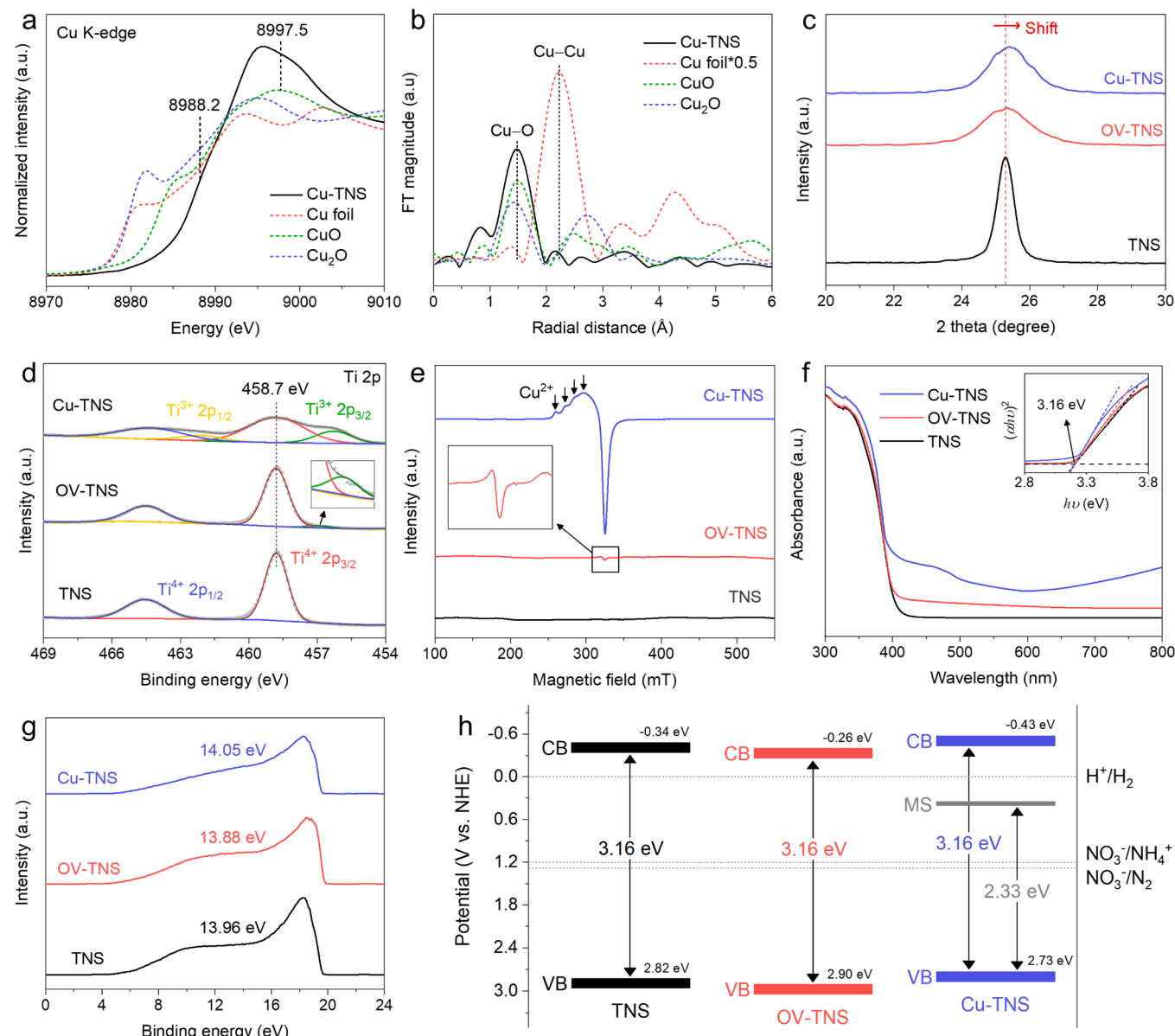


Fig. 2. (a) Cu K-edge XANES spectra and (b) Fourier-transformed *R*-space EXAFS of Cu-TNS with the references (Cu foil, CuO and Cu₂O). (c) Magnified XRD patterns, (d) Ti 2p XPS spectra (inset: enlarged Ti³⁺ 2p_{3/2} peak of OV-TNS), (e) EPR spectra (inset: enlarged EPR spectrum of OV-TNS) and (f) UV-visible DRS spectra (inset: the corresponding Tauc plots using $(\alpha h\nu)^2$ as a function vs. the photon energy, where α is the absorption coefficient, h is the Planck's constant, ν is the light frequency) of TNS, OV-TNS and Cu-TNS. (g) UPS spectra with corresponding peak widths and (h) the band structure alignments in TNS, OV-TNS and Cu-TNS. The bandgap energy (E_g) of Cu-TNS from the Tauc plot is 3.16 eV. The valence band energy values were calculated using He I excitation energy (21.22 eV) and the UPS width. The conduction band energy values were calculated using the obtained bandgap and valence band energies. All energy vs. vacuum values were converted to vs. NHE using the following relationship: $E_{vacuum} = -E_{NHE} - 4.44$ eV.

of Cu foil and Cu₂O. It is noteworthy that the single Cu atoms exhibited a high oxidation state originating from a high unoccupied state level, thereby implying its high electron-accepting capacity. Fourier transformation of the extended X-ray absorption fine structure (EXAFS) of Cu-TNS shows only one characteristic peak at ~ 1.5 Å corresponding to the Cu—O scattering path, indicating that the Cu atoms in the 2+ oxidation state had been stabilized at the Ti sites and were coordinated with the oxygen atoms in the lattice (Fig. 2b). The absence of the Cu—Cu scattering path at ~ 2.2 Å verifies that Cu-TNS was substantially free from Cu clustering.

After acquiring proof of single Cu atoms occupying the Ti sites, the spontaneous formation of OVs and lattice distortion was investigated. The Ti K-edge XANES spectra of TNS, OV-TNS, and Cu-TNS in Fig. S8a and S8b are analogous with three pre-edge peaks associated with

anatase TiO₂ (labeled P1, P2, and P3), corresponding to the enabling of quadruple 1 s→3d transitions [35]. The intensity escalation in P2 for OV-TNS and Cu-TNS implies Ti site distortion due to the introduction of Cu atoms and/or OV into the lattice. By comparing reference Ti configurations with different valence states, the OV concentrations in OV-TNS and Cu-TNS were calculated as 2.21% and 9.89%, respectively (Fig. S9 and Table S1). The abundant OV concentration in Cu-TNS indicates that incorporation of Cu atoms into Ti atomic sites induces spontaneous OV formation due to the different valence states of Ti and Cu. Fourier transformation of the EXAFS spectrum of the *R*-space reveals that the Ti—O scattering path for OV-TNS and Cu-TNS decreased in intensity and shifted to shorter distances, suggesting abatement of the Ti—O coordination number owing to the formation of OV and Ti³⁺ (Fig. S8c). Furthermore, the X-ray diffraction (XRD) patterns of the

prepared photocatalysts in Fig. S10 exhibit typical peaks attributed to anatase TiO_2 (JCPDS-21-1272), with differences in intensity depending on the presence or absence of defects. Interestingly, the anatase (101) reflection plane of Cu-TNS shifted to a higher number of 2θ degrees, strongly implying that the lattice strain had become constricted (Fig. 2c) due to the presence of the interstitial Cu^{2+} sites inside the TiO_2 . The lattice strain was calculated using the Voigt method as -0.705% for Cu-TNS (Table S2), revealing that although the atomic radius of Cu^{2+} (0.73 Å) is larger than that of Ti^{4+} (0.61 Å), Cu atomic incorporation inside the TiO_2 lattice constitutes a negative strain due to OV formation leading to Jahn-Teller compression [35]. Structural defects in the lattice were also evidenced via HAADF-STEM analysis (Figs. S11 and S12). The atomic structure of TNS is well-aligned whereas severe distortion was observed in Cu-TNS. Line scan profiles reveal that the length of the atomic array consisting of both Ti and Cu is shorter than that of the pristine Ti-only atomic array.

The defects in OV-TNS and Cu-TNS were further examined by using X-ray photoelectron spectroscopy (XPS) (Fig. 2d and Fig. S13) and electron paramagnetic resonance (EPR) (Fig. 2e and Fig. S14). The deconvoluted high-resolution Ti 2p XPS spectra of TNS and OV-TNS contain typical characteristic peaks for Ti^{4+} , with that of OV-TNS having a slight rise of additional Ti^{3+} characteristic peaks, which is the result of OV and Ti^{3+} presence. In the case of Cu-TNS, distinct Ti^{3+} peaks appeared, implying higher concentration of OVs and Ti^{3+} due to the incorporation of Cu atoms. The high-resolution O 1s XPS spectra of Cu-TNS are also distinct from OV-TNS and TNS in terms of the shift in lattice oxygen peak and the increased area of OV-associated peak due to the Cu atom incorporation and coordination with neighboring O atoms. The results from the EPR spectra are with those from the XPS analysis by revealing a faint signal for TNS with distinct signals at $g = \sim 1.998$ (OV) and ~ 2.003 (Ti^{3+}) for Cu-TNS. Although the spectrum for OV-TNS likewise shows two signals representing OV and Ti^{3+} , their intensities are noticeably smaller than those in the spectrum for Cu-TNS, which indicates lower concentration of OVs and Ti^{3+} in the absence of Cu atoms. It is noteworthy that the spectrum for Cu-TNS exhibits an asymmetric resonance line arising from the anisotropic hyperfine structure of Cu^{2+} ions, and related EPR simulations further reveal that the asymmetric resonance line consists of two components: interstitial Cu^{2+} sites inside the TiO_2 lattice and the Cu^{2+} species on the surface (Fig. S15). The XPS and EPR results are consistent with the aforementioned XAS, XRD, and HAADF-STEM results, confirming defect formation by the introduction of single Cu atoms.

The optical properties and band structures of the prepared photocatalysts (vital for analyzing their efficiencies) were determined by using UV-visible diffuse reflectance (DRS) and UV photoelectron spectroscopy (UPS). The UV-visible DRS spectra reveal that TNS exhibits a sharp edge at ~ 390 nm, corresponding to the interband transition of anatase TiO_2 (Fig. 2f). Meanwhile, those of OV-TNS and Cu-TNS exhibit enhanced absorption in the visible light region due to the presence of defects. That of Cu-TNS with isolated Cu atoms further exhibits step-like absorption at ~ 480 nm and a broad band at ~ 700 nm, reflecting the generation of the mid-gap state (MS) and $d-d$ transition in Cu [26], respectively. Nevertheless, the estimated intrinsic bandgaps of TNS, OV-TNS, and Cu-TNS were still identical (3.16 eV), as determined from their converted UV-visible spectra (the inset of Fig. 2f). The additional bandgap corresponding to the electronic transition between the valence band (VB) and MS of Cu-TNS was identified as 2.33 eV (Fig. S16). The ionization potential or the VB energy was measured from the UPS spectra in Fig. 2g and Fig. S17 by subtracting the peak width from the He I excitation energy (21.22 eV). The band positions of TNS, OV-TNS, and Cu-TNS were identified by employing the obtained bandgap and VB energy values (vs. NHE), (Fig. 2h). In particular, the conduction band (CB) energy of Cu-TNS is more negative than its counterparts, signifying that PcnRA is more efficient with Cu-TNS from a thermodynamic perspective.

3.2. Photocatalytic NH_4^+ production

The PcnRA experiments were conducted in an aqueous NO_3^- solution under full-spectrum irradiation (see Supporting Information) and mainly quantified using ion chromatography (Figs. S18 and S19). Formic acid (HCOOH) was selected as an electron donor or simulated organic matter due to its abundance in wastewater and its ability for NH_3 synthesis via formation of carboxyl anion radicals with strong reducing capability [14,38]. For optimization of the Cu content, Cu-TNS with various at% of Cu to Ti were synthesized and the actual wt% of Cu was analyzed by inductively coupled plasma atomic emission spectroscopy (Table S3). All of the prepared Cu-TNS samples provided attractive NH_4^+ yields regardless of the at% of Cu (Fig. 3a), as well as optical modulation which may be indicative of a reversible $\text{Cu}^{2+}/\text{Cu}^{1+}$ reduction process (0.16 eV vs. NHE) with lattice tuning by atomically localized photoelectrons at isolated Cu sites (Fig. S20) [26,27]. Among them, the 3 at% (1.95 wt%) Cu sample had the highest NH_4^+ photosynthesis activity and was thus selected for further study. The basis of the relatively inferior activities of the 6 at% and 8 at% Cu samples was the formation of new configurations such as clusters or CuO phases, as unveiled via XAS and XRD analyses (Fig. S21). In addition, Cu metal nanoparticle-deposited TNS (CuNP/TNS) was prepared via a photo-deposition method to explicitly examine the benefits of SAC over metal cluster catalysts for PcnRA. The outcomes of relevant analyses such as TEM, XAS, XRD, and XPS validated the successful synthesis of the CuNP/TNS catalyst (Figs. S22–S24). During the 2-h PcnRA experiment, the three modified TNS catalysts exhibited at least triple the activity of TNS for NH_4^+ production, indicating that the presence of Cu and/or OVs improves the surface catalytic activity of TiO_2 to facilitate NH_3 photosynthesis (Fig. 3b). Notably, the NH_4^+ yield rate of Cu-TNS was significantly increased by 62-fold compared to TNS, demonstrating the impressive effect of SAC on PcnRA. The wavelength-dependent AQY of Cu-TNS showed a trend consistent with the optical absorption spectrum and reached its highest value of 6.1% at 330 nm (Fig. 3c). This consistency secures the knowledge that the reaction is indeed the photo-driven NO_3^- -to- NH_3 conversion of the catalyst, which is further supported by negligible NH_4^+ production in the control experiments (Fig. S25).

Subsequently, the PcnRA selectivity (another pivotal aspect of this study) was investigated (Fig. 3d and Fig. S26). After 24 h of PcnRA employing Cu-TNS, 199.98 μmol of the supplied NO_3^- in the reaction solution was reduced, leaving only 1.15 μmol from the initial amount (201.14 μmol). Meanwhile, 195.06 μmol of NH_4^+ was produced from the NO_3^- reduction process, indicating that most of the N molecules had been selectively converted to NH_4^+ . The NH_4^+ yield rate remained linear for the first few hours but then gradually diminished over time due to the depletion of NO_3^- . The NH_4^+ yield scarcely changed during the last 4 h of the reaction, suggesting that the produced NH_4^+ was not oxidized back to N_2 by the photoholes. Nitrite ions (one of the most common by-products of NO_3^- reduction) [14,22,33] were not detected throughout the reaction, and the total amount of N species remained nearly identical during the reaction, inferring that the only N-specie products of photocatalytic NO_3^- reduction were NH_4^+ and N_2 . Compared with TNS, OV-TNS, and CuNP/TNS exhibit enhanced activity in terms of NO_3^- reduction and selective NH_4^+ production, respectively, demonstrating that the OVs serve as a favorable NO_3^- adsorption site and the Cu species play a decisive role in selective NH_4^+ production. Still, CuNP/TNS provided a considerable N_2 yield compared to Cu-TNS, which can be postulated by the multiple adsorption sites for NO_3^- on the metal particles increasing the possibility of N–N bonding [39]. Cu-TNS exhibits significantly enhanced activity for both NO_3^- reduction and selective NH_4^+ production compared to its counterparts thanks to the synergistic effect of Cu atom incorporation and spontaneous defect formation. Consequently, Cu-TNS achieved 97.6% for NH_4^+ selectivity from an N-specie conversion viewpoint (see Supporting Information) when $> 99\%$ of NO_3^- was consumed (Fig. 3e and Table S4), confirming both selective and outstanding PcnRA performance.

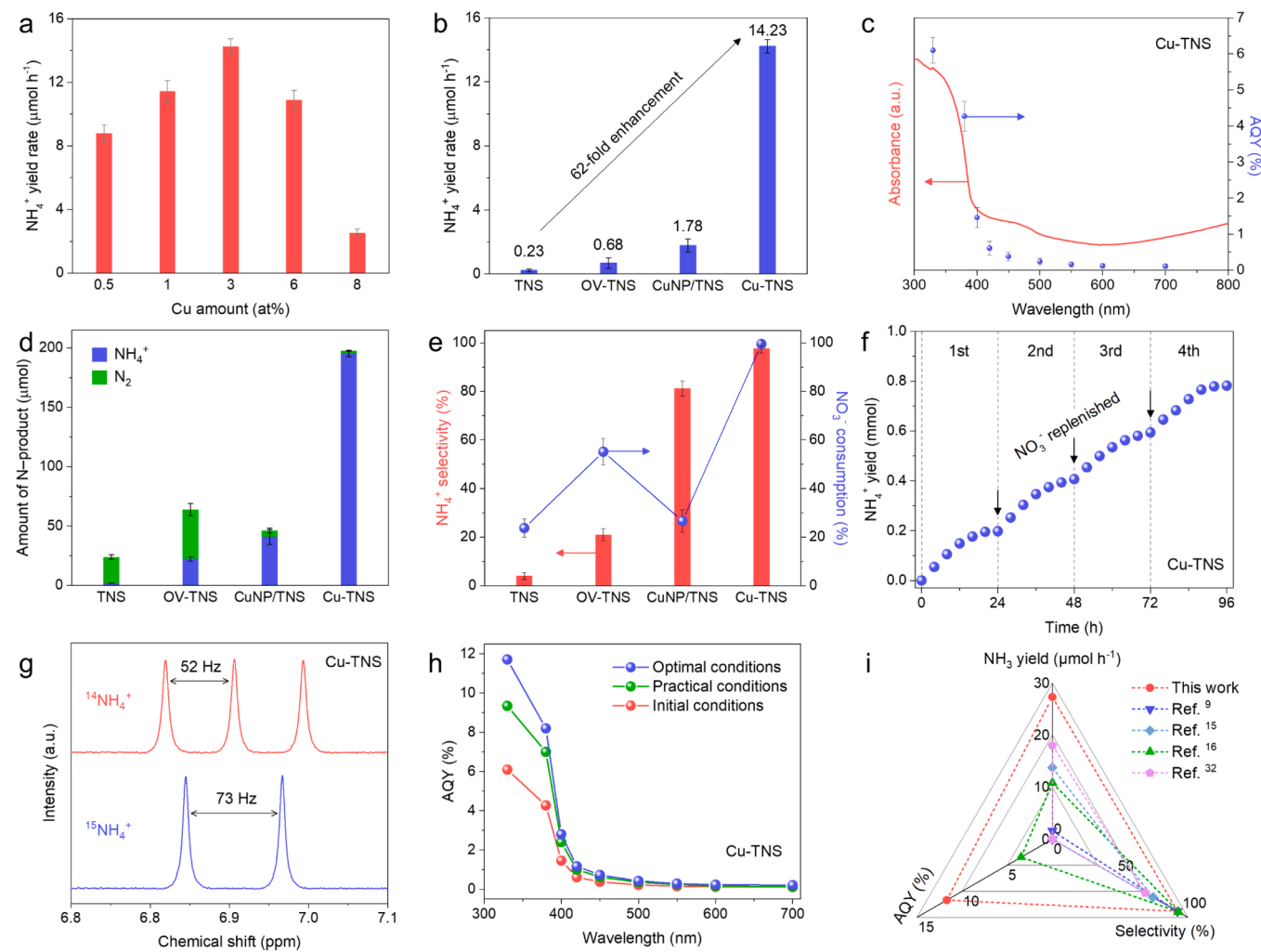


Fig. 3. (a) The NH₄⁺ yield rate of Cu-TNS after the first two hours of PcNRA depending on the Cu amount. (b) The NH₄⁺ yield rate of TNS, OV-TNS, CuNP/TNS and Cu-TNS after the first two hours of PcNRA. (c) Wavelength-dependent AQY of Cu-TNS for PcNRA vs. light absorption. (d) The amounts of N-species products after 24 h of PcNRA. (e) NH₄⁺ selectivity in terms of N-species conversion and NO₃⁻ consumption after 24 h of PcNRA. (f) Long-term PcNRA stability testing of Cu-TNS. The NH₄⁺ yield rate gradually decreased over the 24-hour cycle due to the depletion of NO₃⁻. At the end of each 24-h cycle, NO₃⁻ supplementation restored the yield rate of NH₄⁺ to its initial level. (g) ¹H NMR spectra of the NH₄⁺ generated after 12 h of PcNRA using Cu-TNS with K¹⁴NO₃ and K¹⁵NO₃ as the reactant feedstocks. (h) Wavelength-dependent AQY of Cu-TNS for PcNRA under various reaction conditions. (i) Comparison of NH₃ yield, selectivity, and AQY of Cu-TNS with those of previously reported PcNRA photocatalysts.

NH₄⁺ selectivity from a photocatalytic viewpoint was also assessed by considering the total amount of reacted electrons (including H₂ evolution) (Fig. S27 and Supporting Information). During the initial two hours, the H₂ evolution rate from using Cu-TNS was negligible, and 99.2% NH₄⁺ selectivity was achieved. However, it increased considerably as NO₃⁻ was depleted over time, with NH₄⁺ selectivity eventually reaching 93.5% (Fig. S28). Hence, the H₂ evolution activity of Cu-TNS was further evaluated without NO₃⁻ to verify the correlation between proton reduction and NO₃⁻ abundance (Fig. S29). As expected, the absence of NO₃⁻ significantly improved H₂ production compared to the presence of NO₃⁻, suggesting that abundant NO₃⁻ boosts preferential NO₃⁻ reduction while suppressing H⁺ reduction.

The long-term stability of Cu-TNS was evaluated during four consecutive reaction cycles (Fig. 3f), with NO₃⁻ replenishment at the end of each cycle restoring the diminished NH₄⁺ production rate to its initial level. A similar trend was observed without noticeable degradation for the 96-h reaction of 4 consecutive cycles, indicating that the stabilization of the Cu atoms in the TiO₂ lattice leads to excellent stability, unlike typical SACs suffering from migration, aggregation, or leaching due to high surface energy [40]. Interestingly, the increase in H₂ production activity also declined back to its initial level upon NO₃⁻ replenishment,

again supporting that NO₃⁻ is preferentially reduced on the catalyst surface rather than H⁺ (Fig. S30). The post-characterization of Cu-TNS after the long-term photoreaction provided almost identical results, thereby confirming again the excellent stability and recyclability of Cu-TNS for PcNRA (Fig. S31).

An isotopic labeling experiment using ¹⁴NO₃⁻ and ¹⁵NO₃⁻ as the feedstock was carried out to clarify the N source for the products from the PcNRA. Within 12 h of reaction using the isotopic feedstock, triplet ¹⁴NH₄⁺ and doublet ¹⁵NH₄⁺ signals were distinguishable in the ¹H nuclear magnetic resonance (NMR) spectrum of Cu-TNS, verifying that the supplied NO₃⁻ had been successfully reduced to NH₄⁺ (Fig. 3g). Moreover, the time-dependent increase in the NMR signals and analogous quantification of ¹⁴NH₄⁺ and ¹⁵NH₄⁺ indicate once again that prevalent NH₄⁺ production occurs through PcNRA, implying that the involvement of external N species was negligible (Figs. S32–S34). The produced NH₄⁺ amount after 12 h of the reaction was quantified using assorted methods such as NMR, IC, and colorimetry (Fig. S35). All three techniques provided comparable results and highlighted the validity of our quantification findings. Slight overestimation when using colorimetry may be ascribed to the presence of a hole scavenger reacting with the Nessler reagent [41].

As catalytic activity is highly dependent on the reaction conditions, four sets of optimization experiments to regulate the catalyst dose, NO_3^- amount, sacrificial reagent type, and volume were carried out to maximize the photocatalytic activity and AQY of Cu-TNS (Fig. S36). Consequently, the reaction conditions of 50 mg catalyst, 500 μmol NO_3^- and 10 vol% HCOOH with which Cu-TNS achieved the highest NH_4^+ production rate of 29.81 $\mu\text{mol h}^{-1}$ were found to be optimal and were subsequently selected for obtaining AQY measurements. Furthermore, 0.5 wt% (0.45 vol%) HCOOH was also considered as the organic matter content (<1 wt%) in actual waste water [42,43] (denoted as practical conditions). Compared with the initial conditions, the optimal ones comprehensively improved the AQY of Cu-TNS in the absorption region up to 700 nm under adjusted reaction conditions; the highest AQY of 11.7% at 330 nm together with a solar-to-ammonia conversion efficiency of 0.40% under the optimal conditions (Fig. 3h) shows that it far outperforms the current state-of-the-art photocatalysts for PcnRA (Fig. 3i and Table S5).

3.3. Charge-transfer dynamics

As the photocatalytic performance is closely related to the charge carrier transfer in the catalyst, the mechanistic origins underlying the exceptional PcnRA activity of Cu-TNS were elucidated by probing its interfacial charge dynamics. Steady-state photoluminescence (PL) emission and time-resolved PL (TRPL) spectroscopy were first employed to study the charge-transfer dynamics in the bulk phase in the catalysts (Fig. S37 and Table S6). The quenched PL emission upon the introduction of Cu or OVs suggests the emergence of non-radiative recombination pathways within TNS (electron migration to Cu or OVs). This contention was validated by the hastened PL decay kinetics (shortened average carrier lifetime) due to the presence of Cu and/or OVs, signifying that the charge-transfer dynamics of TNS are accelerated via an additional interfacial charge-transfer pathway. The overall photocatalytic performance could also be governed by the surface charge

dynamics occurring at a relatively slow timescale (μs to ms) [44], which is thus the rate-determining step. In order to paint a clear picture of the surface charge dynamics, in-situ transient absorption (TA) measurements were conducted under the optimal conditions for PcnRA to uncover the actual interaction mechanism between the surface photoelectrons and the reacting species (Fig. 4a and Fig. S38). The wavelength region for the surface photoelectrons was identified as 400 nm, which showed pronounced bleaching recovery in the presence of Ag^+ ions as electron scavengers (Fig. S39). Accordingly, the in-situ TA profiles probed at 400 nm were fitted with a triexponential kinetics equation for quantitative interpretation (Table S7). Notably, the three modified TNS catalysts displayed substantially faster bleaching recovery kinetics than TNS, among which Cu-TNS exhibited the most hastened kinetics for bleaching recovery with an average lifetime (26.2 μs), which is more than one order of magnitude shorter than TNS (526.0 μs). The markedly shortened lifetime of Cu-TNS demonstrates that the surface photoelectrons are expeditiously consumed to participate in the NO_3^- reduction reaction, which accounts for the exceptional PcnRA activity.

The superior photogenerated charge transfer of Cu-TNS was further revealed via a photoelectrochemical (PEC) assessment. The photoelectrode was fabricated using facile electrophoretic deposition on a conductive substrate to avoid altering the intrinsic properties of the powder photocatalysts. The prepared photoelectrode had both uniform thickness and contact with the catalyst, rendering it suitable for the PEC measurements (Fig. S40a). The linear sweep voltammetry curves of Cu-TNS exhibit enhanced current density in the presence of NO_3^- , which is indicative of its capability to reduce NO_3^- (Fig. S40b). Compared with the photoelectrodes made with its counterparts, the Cu-TNS one attained the most positive onset potential, thereby proving its superior NO_3^- reduction performance (Fig. S40c). Likewise, the transient photocurrent density of the Cu-TNS photoelectrode was substantially higher than that of its counterparts due to its higher charge-transfer rate for the surface NO_3^- reduction reaction (Fig. 4b). This consistent conclusion is also evidenced by the electrochemical impedance spectra, in which Cu-TNS

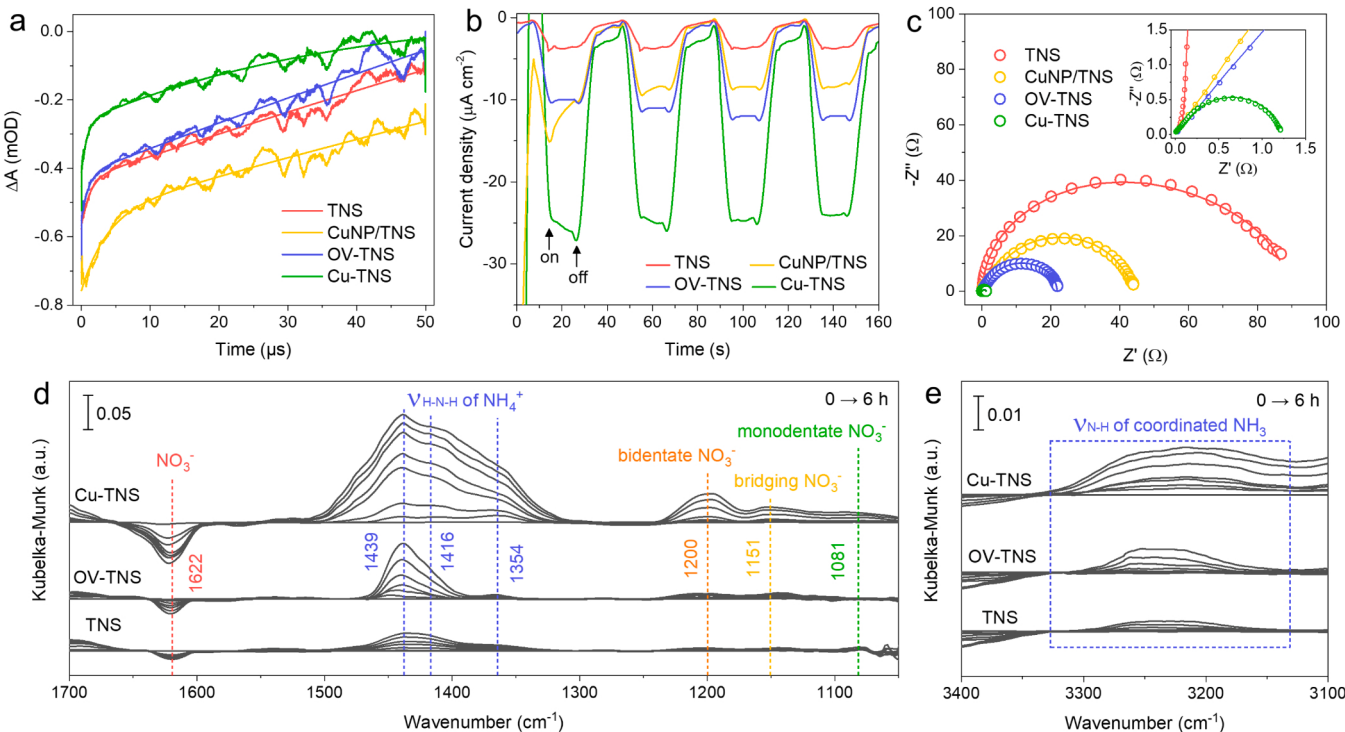


Fig. 4. (a) The TA kinetic profiles of the prepared photocatalysts probed at 400 nm. PEC assessment of the prepared photoelectrodes at -0.6 V vs. Ag/AgCl in aqueous 0.5 M K_2SO_4 solution; (b) transient photocurrent density curves under sequential irradiation with an interval of 20 s on/off switch and (c) electrochemical impedance spectroscopy Nyquist plots under continuous irradiation (inset: enlarged plots showing the full arc of Cu-TNS). *In-situ* DRIFTS spectra of Cu-TNS, OV-TNS and TNS under 6 h of light irradiation in the range of (d) 1700–1050 cm^{-1} and (e) 3400–3100 cm^{-1} .

exhibits the smallest arc radius (charge-transfer resistance, $R_{ct} = 1.22 \Omega$) in the subsequent Nyquist plots, thereby indicating that it provided the most effective separation of the photogenerated charge carriers (Fig. 4c, Fig. S40d and Table S8). The PEC measurements also deliver reasonable evidence for the pronounced charge transfer and the exceptional PcnRA activity of Cu-TNS under photoirradiation, which is in accordance with the above in-situ TA results.

3.4. Photocatalytic reaction mechanism

Afterward, to dynamically investigate the reaction mechanism of PcnRA, in-situ diffuse reflectance infrared Fourier transform spectroscopy (DRIFTS) analysis of the NO_3^- -adsorbed catalysts was conducted under continuous irradiation. The spectra for Cu-TNS exhibit noticeable attenuation of the absorption band at 1622 cm^{-1} corresponding to the adsorbed NO_3^- species [14] whereas that in the OV-TNS spectra was only marginal and that in the TNS spectra was even less than OV-TNS (Fig. 4d). Moreover, the spectra of Cu-TNS show distinctive absorption bands at 1200, 1151, and 1081 cm^{-1} , which were assigned to activated NO_3^- species in the bidentate [45], bridging [22] and monodentate [22] coordination modes, respectively. On the other hand, the TNS spectra barely show the absorption bands corresponding to the activated NO_3^- species, and the OV-TNS spectra show a slight increase in the corresponding absorption bands. These results evidently imply that the adsorption of NO_3^- is accelerated due to the presence of OV in the catalyst surface and can be readily activated for the subsequent reduction

process. Moreover, the simultaneous presence of isolated Cu atoms and OV even further stimulates this process, achieving the more hastened NO_3^- adsorption and activation. In particular, the steady and substantial increase in the absorption bands at 1439, 1416, and 1354 cm^{-1} assigned to the H–N–H stretching vibration [14,22] infers the selective production of NH_4^+ via PcnRA, which explicitly appeared in the spectra for Cu-TNS. The efficient NH_4^+ production of Cu-TNS was also validated by a specific band in the range of $3300\text{--}3100 \text{ cm}^{-1}$, which is widely accepted as the N–H stretching vibration in coordinated NH_3 species [46,47] (Fig. 4e). In contrast, the insignificant rise in NH_4^+ -associated absorption bands in TNS reflects inferior and non-selective PcnRA activity because of no single Cu atoms and surface defects. Meanwhile, the OV-TNS spectrum shows slightly increased NH_4^+ -associated absorption bands compared to TNS but considerably less than Cu-TNS, indicating the significance of isolated Cu atoms on the catalyst surface for PcnRA. Thus, the in-situ DRIFTS results firmly prove that NO_3^- is favorably adsorbed and activated in the presence of isolated Cu atoms and surface defects and then ultimately reduced to NH_4^+ .

To gain deeper insight into the effect of Cu single-atoms on the enhanced photocatalytic activity, density functional theory (DFT) calculations were performed using different local geometries of the anatase TiO_2 (001) surface models such as single-atom Cu-incorporated TiO_2 ($\text{Cu}-\text{TiO}_2$), $\text{Cu}-\text{TiO}_2$ with OV ($\text{Cu}-\text{TiO}_2\text{-OV}$) and partially hydrogenated $\text{Cu}-\text{TiO}_2$ ($\text{Cu}-\text{TiO}_2\text{-H}$) (Fig. S41). The spin-polarized projected density of states (Fig. 5a–c and Fig. S42) and the corresponding photoelectron-transfer pathway schematics (Fig. 5d) based on hybrid functional

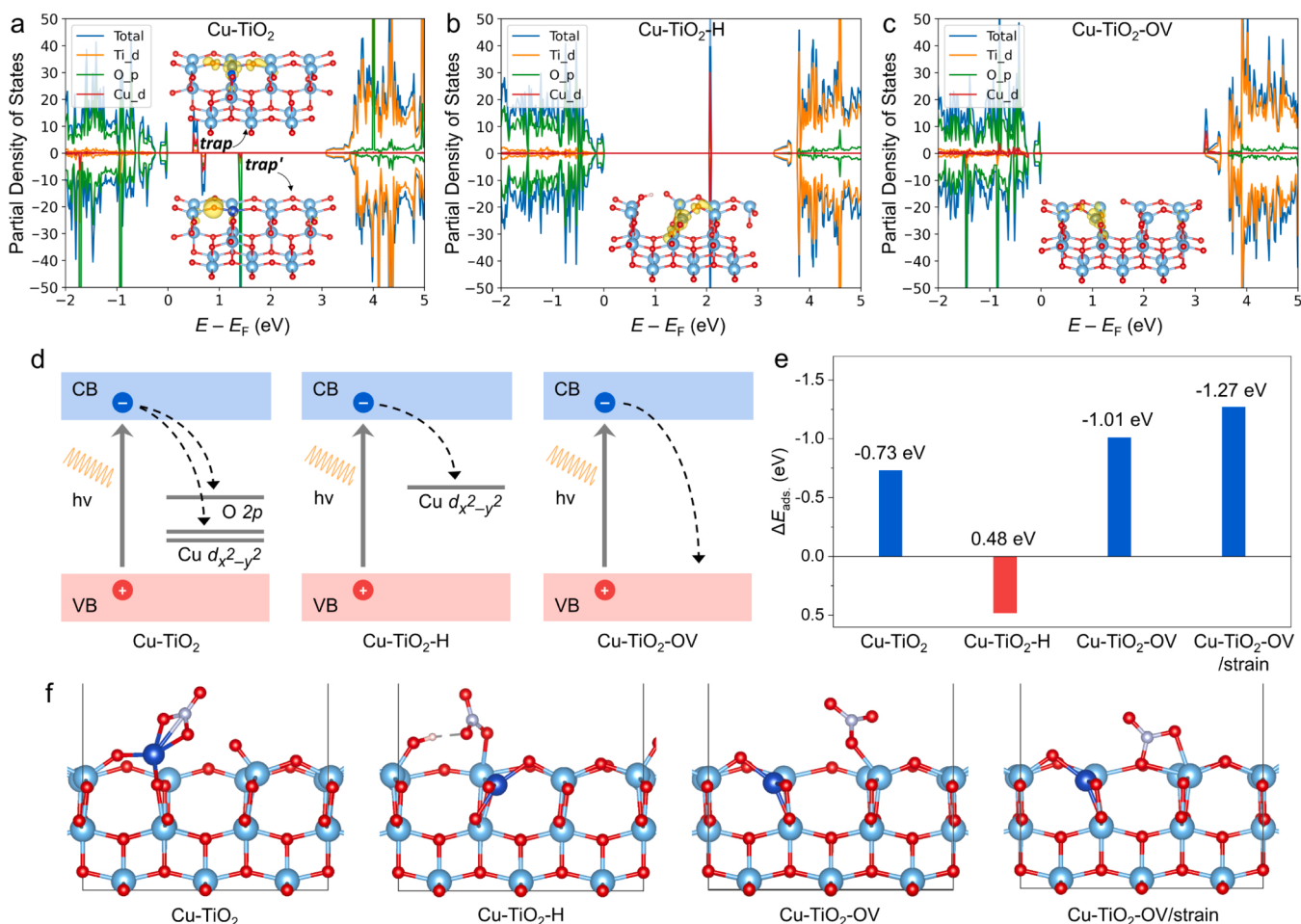


Fig. 5. PDOS of (a) $\text{Cu}-\text{TiO}_2$, which contains one spin-up trap state and two spin-down trap states, (b) $\text{Cu}-\text{TiO}_2\text{-H}$, which has a mid-gap trap state within band gap and (c) $\text{Cu}-\text{TiO}_2\text{-OV}$, which shows the shallow trap state near CB minimum (inset: the DFT-optimized atomic structure for each state). (d) Schematics of the electron transfer process for each state after photoexcitation of charge carriers. (e) Adsorption energies and (f) configurations of NO_3^- on the anatase TiO_2 (001) surface of each state.

calculations elucidate that the Cu atom in a Ti vacancy provides three trap states which were primarily derived from the O 2p orbitals (marked as *trap'*) and the Cu $d_{x^2-y^2}$ orbital (marked as *trap*). Interestingly, when an H atom is favorably adsorbed on the two-coordinated surface O site (adsorption energy, $\Delta E_{ads.} = -3.59$ eV) in the aqueous medium where the PcnRA reaction takes place, the spin-up and spin-down channels form one mid-gap trap state at 2.07 eV. This single mid-gap state, mainly contributed by the Cu $d_{x^2-y^2}$ orbital, enhances the visible light absorption and accumulates the photoelectrons, leading to efficient charge separation. By contrast, only the shallow trap state was left near the CB minimum when OV was introduced at the O site neighboring the Cu atom. Moreover, the first deoxidation of NO_3^- is typically regarded as the rate-determining step in NO_3^- reduction, and thus the strength of NO_3^- adsorption on the catalyst is highly correlated with the overall reaction rate [48]. Therefore, the adsorption energies and configurations of NO_3^- on each surface model were examined as shown in Fig. 5e and f. The NO_3^- adsorption on the TiO_2 (001) surface is favored in bidentate mode irrespective of local geometry, among which the Cu-TiO₂-OV strongly stabilizes the NO_3^- adsorption ($\Delta E_{ads.} = -1.04$ eV) compared to the other surfaces (Cu-TiO₂, $\Delta E_{ads.} = -0.73$ eV and Cu-TiO₂-H, $\Delta E_{ads.} =$

0.48 eV). Notably, the NO_3^- adsorption is even further enhanced to -1.27 eV when the compressive strain of 0.705% is introduced into Cu-TiO₂-OV (denoted as Cu-TiO₂-OV/strain). It is noteworthy that NO_3^- is favorably adsorbed on isolated Cu atoms of the Cu-TiO₂ surface, but favorably adsorbed on Ti atoms adjacent to Cu atoms once OV is introduced to the surface (Cu-TiO₂-OV and Cu-TiO₂-OV/strain). The strong and unitary site-specific NO_3^- adsorption on Ti atoms adjacent to isolated Cu atoms and OV can effectively suppress the release of the intermediate (NO_2^-) during the reduction process and the multiple adsorption of NO_3^- at a single site, reducing the N-N interaction to ensure high selectivity for NH_3 [14]. Our DFT results clearly demonstrate the different roles and contributions of each defect and strain induced in Cu-TNS. The H defect forms the mid-gap state promoting the light absorption and the charge separation, while OV and strain enhance the NO_3^- adsorption.

Here, the PcnRA reaction mechanism on Cu-TNS is proposed on the basis of the aforementioned analyses (Fig. 6). Initially, TiO_2 generates electron-hole pairs under light irradiation. The photogenerated holes, which are readily consumed for organic pollutant decomposition (e.g., HCOOH), facilitate the reaction kinetics. Meanwhile, the aqueous

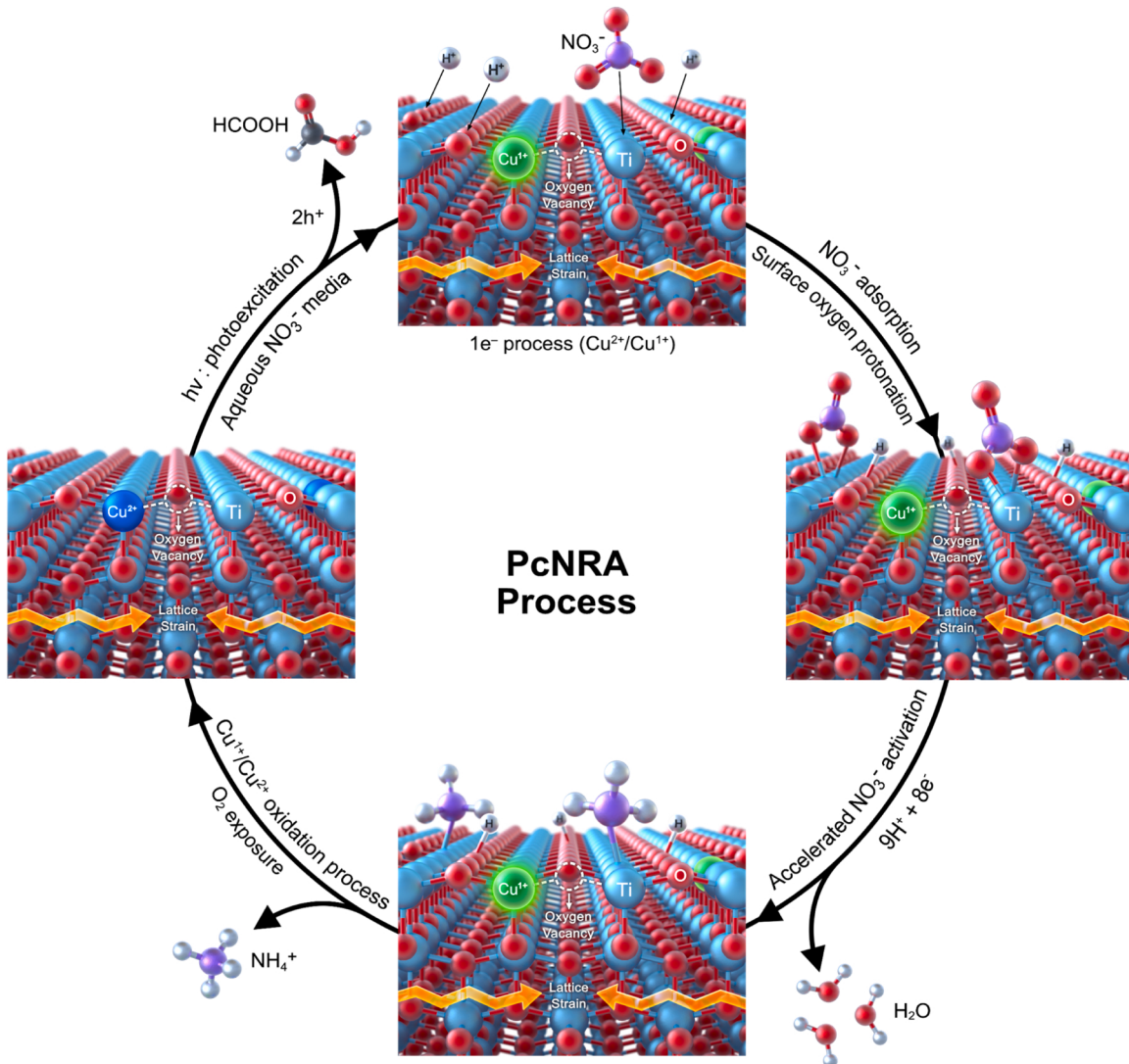


Fig. 6. PcnRA process mechanism on Cu-TNS. TiO_2 with isolated Cu^{2+} atomic sites (blue) and defects generate photoexcited electrons and holes under light irradiation. The photoholes are consumed by HCOOH while the photoelectrons are localized at the Cu sites, reducing Cu^{2+} to Cu^{1+} (green glow). NO_3^- is adsorbed site-specifically on the TiO_2 surface in which oxygen is protonated by the aqueous medium. Defects accelerate the activation of NO_3^- , which is readily reduced to NH_3 via the $9\text{H}^+ + 8\text{e}^-$ processes. The NH_3 is desorbed and preserved in the ionized form of NH_4^+ in an aqueous medium. O_2 purging in the dark restores the Cu valence to its initial state.

medium easily protonates the surface oxygen, leaving a single trap state contributed by the *d* orbitals of the isolated Cu atoms. The electrons migrate from the CB of TiO₂ and become specifically localized in the *d*_{x²-y²} state of the isolated Cu atoms. Thus, efficient charge separation occurs and the accumulated electrons tune the valence state of the Cu atoms and optical modulation occurs. The defects configured adjacent to the Cu atoms induce strong site-specific adsorption of NO₃⁻, reducing the possibility of N–N bonding (an interaction between liberated intermediates) and promptly activating them into the bidentate coordination mode. The coordinated NO₃⁻ is reduced to NH₃ and H₂O is released via 9 H⁺ and 8e⁻ processes, which ultimately ionize to form NH₄⁺ in an aqueous medium. The changed valence state of Cu atoms can be simply restored by exposure to O₂ without light irradiation. Consequently, the efficient charge separation and facilitated NO₃⁻ adsorption/activation synergistically accelerate the NO₃⁻ reduction kinetics to effectively photosynthesize NH₃.

4. Conclusion

We report a highly active and photochemically stable Cu-TNS photocatalyst for selective NH₃ production via NO₃⁻ reduction under ambient conditions. A simple solvothermal method successfully distributed single Cu atoms into Ti vacancies in the TiO₂ matrix, spontaneously forming defects such as OV and lattice strain due to the different valence states and sizes of Ti and Cu. The isolated and stabilized Cu atomic sites accumulate photoelectrons, which inhibits charge carrier recombination and allows more electrons to participate in the reduction reaction, while the structural defects eliminate the NO₃⁻ activation barrier, which facilitates the reduction reaction. Evidence from a series of experiments together with DFT calculations strongly supports the synergistic effect of single Cu atoms and spontaneously formed structural defects in the TiO₂ lattice in terms of enhanced light absorption, efficient charge separation and accelerated NO₃⁻ adsorption/activation. The Cu-TNS photocatalyst achieved 97.6% selectivity for NH₃, a 62-fold enhancement in catalytic activity over TNS, an AQY of 11.7% at 330 nm and a solar-to-ammonia conversion efficiency of 0.40% for NH₃ photosynthesis. Our investigation clearly demonstrates for the first time the impressive impact of SAC along with defect formation on PcnRA, thereby providing the future landscapes of green NH₃ production.

CRediT authorship contribution statement

Hyun Sik Moon: Conceptualization, Methodology, Validation, Formal analysis, Investigation, Writing – original draft, Writing – review & editing, Visualization. **Byeongju Song:** Investigation, Validation. **Jiwon Jeon:** Investigation, Writing – original draft. **Ting-Hsuan Lai:** Investigation, Writing – original draft. **Yu-Peng Chang:** Investigation, Writing – original draft. **Yi-Dong Lin:** Investigation. **Jun Kue Park:** Investigation, Validation, Formal analysis, Writing – original draft. **Yan-Gu Lin:** Formal analysis, Validation. **Yung-Jung Hsu:** Formal analysis, Validation, Writing – review & editing. **Hyeyoung Shin:** Formal analysis, Validation, Writing – review & editing. **Yongju Yun:** Formal analysis, Validation, Data curation. **Kijung Yong:** Supervision, Funding acquisition, Project administration, Writing – review & editing.

Declaration of Competing Interest

The authors declare that they have no known competing financial interests or personal relationships that could have appeared to influence the work reported in this paper.

Data Availability

Data will be made available on request.

Acknowledgments

This work was supported by the National Research Foundation of Korea (NRF) grant funded by the Korean government (MSIT) (NRF-2021R1A5A1084921, NRF-2021K1A4A8A02079226).

Appendix A. Supporting information

Supplementary data associated with this article can be found in the online version at doi:10.1016/j.apcatb.2023.123185.

References

- [1] W. Guo, K. Zhang, Z. Liang, R. Zou, Q. Xu, Electrochemical nitrogen fixation and utilization: theories, advanced catalyst materials and system design, *Chem. Soc. Rev.* 48 (2019) 5658–5716, <https://doi.org/10.1039/C9CS00159J>.
- [2] W. Chen, X. Yang, Z. Chen, Z. Ou, J. Hu, Y. Xu, Y. Li, X. Ren, S. Ye, J. Qiu, J. Liu, Q. Zhang, Emerging applications, developments, prospects, and challenges of electrochemical nitrate-to-ammonia conversion, *Adv. Funct. Mater.* (2023), 2300512, <https://doi.org/10.1002/adfm.202300512>.
- [3] Y. Ren, C. Yu, L. Wang, X. Tan, Z. Wang, Q. Wei, Y. Zhang, J. Qiu, Microscopic-level insights into the mechanism of enhanced NH₃ synthesis in plasma-enabled cascade N2 oxidation-electroreduction system, *J. Am. Chem. Soc.* 144 (2022) 10193–10200, <https://doi.org/10.1021/jacs.2c00089>.
- [4] C. Gao, T. Wei, Y. Zhang, X. Song, Y. Huan, H. Liu, M. Zhao, J. Yu, X. Chen, A photoresponsive rutile TiO₂ heterojunction with enhanced electron-hole separation for high-performance hydrogen evolution, *Adv. Mater.* 31 (2019), 1806596, <https://doi.org/10.1002/adma.201806596>.
- [5] T.-N. Ye, S.-W. Park, Y. Lu, J. Li, M. Sasase, M. Kitano, T. Tada, H. Hosono, Vacancy-enabled N2 activation for ammonia synthesis on an Ni-loaded catalyst, *Nature* 583 (2020) 391–395, <https://doi.org/10.1038/s41586-020-2464-9>.
- [6] S. Ye, Z. Chen, G. Zhang, W. Chen, C. Peng, X. Yang, L. Zheng, Y. Li, X. Ren, H. Cao, D. Xue, J. Qiu, Q. Zhang, J. Liu, Elucidating the activity, mechanism and application of selective electrosynthesis of ammonia from nitrate on cobalt phosphide, *Energy Environ. Sci.* 15 (2022) 760–770, <https://doi.org/10.1039/DIEE03097C>.
- [7] P. Shen, X. Li, Y. Luo, N. Zhang, X. Zhao, K. Chu, Ultra-efficient N2 electroreduction achieved over a rhodium single-atom catalyst (Rh1/MnO2) in water-in-salt electrolyte, *Appl. Catal. B Environ.* 316 (2022), 121651, <https://doi.org/10.1016/j.apcatb.2022.121651>.
- [8] Y. Xu, K. Ren, T. Ren, M. Wang, Z. Wang, X. Li, L. Wang, H. Wang, Ultralow-content Pd in-situ incorporation mediated hierarchical defects in corner-etched Cu20 octahedra for enhanced electrocatalytic nitrate reduction to ammonia, *Appl. Catal. B Environ.* 306 (2022), 121094, <https://doi.org/10.1016/j.apcatb.2022.121094>.
- [9] J. Choi, B.H.R. Suryanto, D. Wang, H.L. Du, R.Y. Hodgetts, F.M. Ferrero Vallana, D. R. MacFarlane, A.N. Simonov, Identification and elimination of false positives in electrochemical nitrogen reduction studies, *Nat. Commun.* 11 (1) (2020) 10, <https://doi.org/10.1038/s41467-020-19130-z>.
- [10] S.Z. Andersen, V. Colić, S. Yang, J.A. Schwalbe, A.C. Nielander, J.M. McEnaney, K. Enemark-Rasmussen, J.G. Baker, A.R. Singh, B.A. Rohr, M.J. Statt, S.J. Blair, S. Mezzavilla, J. Kibsgaard, P.C.K. Vesborg, M. Cargnello, S.F. Bent, T.F. Jaramillo, I.E.L. Stephens, J.K. Norskov, I. Chorkendorff, A rigorous electrochemical ammonia synthesis protocol with quantitative isotope measurements, *Nature* 570 (2019) 504–508, <https://doi.org/10.1038/s41586-019-1260-x>.
- [11] G.-F. Chen, Y. Yuan, H. Jiang, S.-Y. Ren, L.-X. Ding, L. Ma, T. Wu, J. Lu, H. Wang, Electrochemical reduction of nitrate to ammonia via direct eight-electron transfer using a copper-molecular solid catalyst, *Nat. Energy* 5 (2020) 605–613, <https://doi.org/10.1038/s41560-020-0654-1>.
- [12] H.O. Tugaoen, P. Herckes, K. Hristovski, P. Westerhoff, Influence of ultraviolet wavelengths on kinetics and selectivity for N-gases during TiO₂ photocatalytic reduction of nitrate, *Appl. Catal. B Environ.* 220 (2018) 597–606, <https://doi.org/10.1016/j.apcatb.2017.08.078>.
- [13] N.C. Kani, J.A. Gauthier, A. Prajapati, J. Edgington, I. Bordawekar, W. Shields, M. Shields, L.C. Seitz, A.R. Singh, M.R. Singh, Solar-driven electrochemical synthesis of ammonia using nitrate with 11% solar-to-fuel efficiency at ambient conditions, *Energy Environ. Sci.* 14 (2021) 6349–6359, <https://doi.org/10.1039/DIEE01879E>.
- [14] H. Hirakawa, M. Hashimoto, Y. Shiraishi, T. Hirai, Selective nitrate-to-ammonia transformation on surface defects of titanium dioxide photocatalysts, *ACS Catal.* 7 (2017) 3713–3720, <https://doi.org/10.1021/acscatal.7b00611>.
- [15] J. Lim, C.-Y. Liu, J. Park, Y.-H. Liu, T.P. Senftle, S.W. Lee, M.C. Hatzell, Structure sensitivity of Pd facets for enhanced electrochemical nitrate reduction to ammonia, *ACS Catal.* 11 (2021) 7568–7577, <https://doi.org/10.1021/acscatal.1c01413>.
- [16] H.S. Moon, K.-C. Hsiao, M.-C. Wu, Y. Yun, Y.-J. Hsu, K. Yong, Spatial separation of cocatalysts on Z-Scheme ORganic/inorganic Heterostructure Hollow Spheres for Enhanced Photocatalytic H₂ evolution and in-depth analysis of the charge-transfer mechanism, *Adv. Mater.* 35 (2023), 2200172, <https://doi.org/10.1002/adma.202200172>.
- [17] L. Barrera, R. Bala Chandran, Harnessing photoelectrochemistry for wastewater nitrate treatment coupled with resource recovery, *ACS Sustain. Chem. Eng.* 9 (2021) 3688–3701, <https://doi.org/10.1021/acssuschemeng.0c07935>.

- [18] L. Wang, W. Fu, Y. Zhuge, J. Wang, F. Yao, W. Zhong, X. Ge, Synthesis of polyoxometalates (POM)/TiO₂/Cu and removal of nitrate nitrogen in water by photocatalysis, *Chemosphere* 278 (2021), 130298, <https://doi.org/10.1016/j.chemosphere.2021.130298>.
- [19] D. Sun, W. Yang, L. Zhou, W. Sun, Q. Li, J.K. Shang, The selective deposition of silver nanoparticles onto {101} facets of TiO₂ nanocrystals with co-exposed {001}/{101} facets, and their enhanced photocatalytic reduction of aqueous nitrate under simulated solar illumination, *Appl. Catal. B Environ.* 182 (2016) 85–93, <https://doi.org/10.1016/j.apcatb.2015.09.005>.
- [20] H. Kominami, A. Furusho, S. Murakami, H. Inoue, Y. Kera, B. Ohtani, Effective photocatalytic reduction of nitrate to ammonia in an aqueous suspension of metal-loaded titanium(IV) oxide particles in the presence of oxalic acid, *Catal. Lett.* 76 (2001) 31–34, <https://doi.org/10.1023/A:1016771908609>.
- [21] M. Yamauchi, R. Abe, T. Tsukuda, K. Kato, M. Takata, Highly selective ammonia synthesis from nitrate with photocatalytically generated hydrogen on CuPd/TiO₂, *J. Am. Chem. Soc.* 133 (2011) 1150–1152, <https://doi.org/10.1021/ja106285p>.
- [22] J. Li, R. Chen, J. Wang, Y. Zhou, G. Yang, F. Dong, Subnanometric alkaline-earth oxide clusters for sustainable nitrate to ammonia photosynthesis, *Nat. Commun.* 13 (2022), 1098, <https://doi.org/10.1038/s41467-022-28740-8>.
- [23] H.-T. Ren, S.-Y. Jia, J.-J. Zou, S.-H. Wu, X. Han, A facile preparation of Ag2O/P25 photocatalyst for selective reduction of nitrate, *Appl. Catal. B Environ.* 176–177 (2015) 53–61, <https://doi.org/10.1016/j.apcatb.2015.03.038>.
- [24] B. Qiao, A. Wang, X. Yang, L.F. Allard, Z. Jiang, Y. Cui, J. Liu, J. Li, T. Zhang, Single-atom catalysis of CO oxidation using Pt1/FeOx, *Nat. Chem.* 3 (2011) 634–641, <https://doi.org/10.1038/nchem.1095>.
- [25] N. Daelman, M. Capdevila-Cortada, N. López, Dynamic charge and oxidation state of Pt/CeO₂ single-atom catalysts, *Nat. Mater.* 18 (2019) 1215–1221, <https://doi.org/10.1038/s41563-019-0444-y>.
- [26] B.-H. Lee, S. Park, M. Kim, A.K. Sinha, S.C. Lee, E. Jung, W.J. Chang, K.-S. Lee, J. H. Kim, S.-P. Cho, H. Kim, K.T. Nam, T. Hyeon, Reversible and cooperative photoactivation of single-atom Cu/TiO₂ photocatalysts, *Nat. Mater.* 18 (2019) 620–626, <https://doi.org/10.1038/s41563-019-0344-1>.
- [27] Y. Zhang, J. Zhao, H. Wang, B. Xiao, W. Zhang, X. Zhao, T. Lv, M. Thangamuthu, J. Zhang, Y. Guo, J. Ma, L. Lin, J. Tang, R. Huang, Q. Liu, Single-atom Cu anchored catalysts for photocatalytic renewable H₂ production with a quantum efficiency of 56%, *Nat. Commun.* 13 (2022), 58 <https://doi.org/10.1038/s41467-021-27698-3>.
- [28] S. Hejazi, S. Mohajernia, B. Osuagwu, G. Zopellaro, P. Andryskova, O. Tomanec, S. Kment, R. Zboril, P. Schmuki, On the controlled loading of single platinum atoms as a Co-Catalyst on TiO₂ anatase for optimized photocatalytic H₂ generation, *Adv. Mater.* 32 (2020), 1908505, <https://doi.org/10.1002/adma.201908505>.
- [29] E. Lam, K. Larmier, P. Wolf, S. Tada, O.V. Safonova, C. Copéret, Isolated Zr surface sites on silica promote hydrogenation of CO₂ to CH₃OH in supported Cu catalysts, *J. Am. Chem. Soc.* 140 (2018) 10530–10535, <https://doi.org/10.1021/jacs.8b05595>.
- [30] Y. Yin, L. Shi, W. Li, X. Li, H. Wu, Z. Ao, W. Tian, S. Liu, S. Wang, H. Sun, Boosting Fenton-like reactions via single atom Fe catalysis, *Environ. Sci. Technol.* 53 (2019) 11391–11400, <https://doi.org/10.1021/acs.est.9b03342>.
- [31] K. Fujiwara, S.E. Pratsinis, Single Pd atoms on TiO₂ dominate photocatalytic NO_x removal, *Appl. Catal. B Environ.* 226 (2018) 127–134, <https://doi.org/10.1016/j.apcatb.2017.12.042>.
- [32] H. Wan, A. Bagger, J. Rossmeisl, Electrochemical nitric oxide reduction on metal surfaces, *Angew. Chem. Int. Ed.* 60 (2021) 21966–21972, <https://doi.org/10.1002/anie.202108575>.
- [33] Q. Hu, Y. Qin, X. Wang, Z. Wang, X. Huang, H. Zheng, K. Gao, H. Yang, P. Zhang, M. Shao, C. He, Reaction intermediate-mediated electrocatalyst synthesis favors specified facet and defect exposure for efficient nitrate–ammonia conversion, *Energy Environ. Sci.* 14 (2021) 4989–4997, <https://doi.org/10.1039/D1EE01731D>.
- [34] X. Chen, L. Liu, P.Y. Yu, S.S. Mao, Increasing solar absorption for photocatalysis with black hydrogenated titanium dioxide nanocrystals, *Science* 331 (2011) 746–750, <https://doi.org/10.1126/science.1200448>.
- [35] Y. Zhao, Y. Zhao, R. Shi, B. Wang, G.I.N. Waterhouse, L.-Z. Wu, C.-H. Tung, T. Zhang, Tuning oxygen vacancies in ultrathin TiO₂ nanosheets to boost photocatalytic nitrogen fixation up to 700 nm, *Adv. Mater.* 31 (2019), 1806482, <https://doi.org/10.1002/adma.201806482>.
- [36] Z. Gong, W. Zhong, Z. He, Q. Liu, H. Chen, D. Zhou, N. Zhang, X. Kang, Y. Chen, Regulating surface oxygen species on copper (I) oxides via plasma treatment for effective reduction of nitrate to ammonia, *Appl. Catal. B Environ.* 305 (2022), 121021, <https://doi.org/10.1016/j.apcatb.2021.121021>.
- [37] X. Han, Q. Kuang, M. Jin, Z. Xie, L. Zheng, Synthesis of titania nanosheets with a high percentage of exposed (001) facets and related photocatalytic properties, *J. Am. Chem. Soc.* 131 (2009) 3152–3153, <https://doi.org/10.1021/ja8092373>.
- [38] N. Tong, Y. Wang, Y. Liu, M. Li, Z. Zhang, H. Huang, T. Sun, J. Yang, F. Li, X. Wang, PdSn/NiO/NaTaO₃:La for photocatalytic ammonia synthesis by reduction of NO₃⁻ with formic acid in aqueous solution, *J. Catal.* 361 (2018) 303–312, <https://doi.org/10.1016/j.jcat.2018.03.013>.
- [39] Z. Teng, Q. Zhang, H. Yang, K. Kato, W. Yang, Y.-R. Lu, S. Liu, C. Wang, A. Yamakata, C. Su, B. Liu, T. Ohno, Atomically dispersed antimony on carbon nitride for the artificial photosynthesis of hydrogen peroxide, *Nat. Catal.* 4 (2021) 374–384, <https://doi.org/10.1038/s41929-021-00605-1>.
- [40] H. Hu, J. Wang, P. Tao, C. Song, W. Shang, T. Deng, J. Wu, Stability of single-atom catalysts for electrocatalysis, *J. Mater. Chem. A* 10 (2022) 5835–5849, <https://doi.org/10.1039/D1TA08582D>.
- [41] Y. Zhao, R. Shi, X. Bian, C. Zhou, Y. Zhao, S. Zhang, F. Wu, G.I.N. Waterhouse, L. Z. Wu, C.H. Tung, T. Zhang, Ammonia detection methods in photocatalytic and electrocatalytic experiments: how to improve the reliability of NH₃ production rates? *Adv. Sci.* 6 (2019), 1802109 <https://doi.org/10.1002/advs.201802109>.
- [42] S. Murgolo, S. Franz, H. Arab, M. Bestetti, E. Falletta, G. Mascolo, Degradation of emerging organic pollutants in wastewater effluents by electrochemical photocatalysis on nanostructured TiO₂ meshes, *Water Res.* 164 (2019), 114920, <https://doi.org/10.1016/j.watres.2019.114920>.
- [43] B. Petrie, R. Barden, B. Kasprzyk-Hordern, A review on emerging contaminants in wastewaters and the environment: current knowledge, understudied areas and recommendations for future monitoring, *Water Res.* 72 (2015) 3–27, <https://doi.org/10.1016/j.watres.2014.08.053>.
- [44] K. Takanabe, Photocatalytic water splitting: quantitative approaches toward photocatalyst by design, *ACS Catal.* 7 (2017) 8006–8022, <https://doi.org/10.1021/acscatal.7b02662>.
- [45] W. Cui, J. Li, F. Dong, Y. Sun, G. Jiang, W. Cen, S.C. Lee, Z. Wu, Highly efficient performance and conversion pathway of photocatalytic NO oxidation on SrO-Clusters@Amorphous carbon nitride, *Environ. Sci. Technol.* 51 (2017) 10682–10690, <https://doi.org/10.1021/acs.est.7b00974>.
- [46] H. Hirakawa, M. Hashimoto, Y. Shiraishi, T. Hirai, Photocatalytic conversion of nitrogen to ammonia with water on surface oxygen vacancies of titanium dioxide, *J. Am. Chem. Soc.* 139 (2017) 10929–10936, <https://doi.org/10.1021/jacs.7b06634>.
- [47] D. Wang, L. Zhang, K. Kamasamudram, W.S. Epling, In situ-DRIFTS study of selective catalytic reduction of NO_x by NH₃ over Cu-exchanged SAPO-34, *ACS Catal.* 3 (2013) 871–881, <https://doi.org/10.1021/cs300843k>.
- [48] Y. Wang, A. Xu, Z. Wang, L. Huang, J. Li, F. Li, J. Wicks, M. Luo, D.-H. Nam, C.-S. Tan, Y. Ding, J. Wu, Y. Lum, C.-T. Dinh, D. Sinton, G. Zheng, E.H. Sargent, Enhanced nitrate-to-ammonia activity on copper–nickel alloys via tuning of intermediate adsorption, *J. Am. Chem. Soc.* 142 (2020) 5702–5708, <https://doi.org/10.1021/jacs.9b13347>.